JCIM JOURNAL OF CHEMICAL INFORMATION AND MODELING

pubs.acs.org/jcim Article

Mechanism of Regio- and Enantioselective Hydroxylation of Arachidonic Acid Catalyzed by Human CYP2E1: A Combined Molecular Dynamics and Quantum Mechanics/Molecular Mechanics Study

Honghui Zhang and Hajime Hirao*

Cite This: J. Chem. Inf. Model. 2025, 65, 2080−2092 Read Online

ACCESS | Metrics & More | Article Recommendations | Supporting Information

ABSTRACT: Regio- and enantioselective hydroxylation of free fatty acids by human cytochrome P450 2E1 (CYP2E1) plays an important role in metabolic regulation and has significant pathological implications. Despite extensive research, the detailed hydroxylation mechanism of CYP2E1 remains incompletely understood. To clarify the origins of regioselectivity and enantioselectivity observed for CYP2E1-mediated fatty acid hydroxylation, molecular dynamics (MD) simulations and quantum mechanics/molecular mechanics (QM/MM) calculations were performed. MD simulations provided key insights into the proximity of arachidonic acid's carbon atoms to the reactive iron(IV)-oxo moiety in compound I (Cpd I), with the ω-1 position being closest, indicating higher reactivity at this site. QM/MM calculations identified hydrogen abstraction as the rate-determining step, with the ω-1*S* transition state exhibiting the lowest energy barrier, consistent with experimentally observed enantioselectivity. Energy decomposition analysis revealed that variations in quantum mechanical energy (ΔE_{QM}) significantly influence reaction barriers, with the most efficient hydrogen abstraction occurring at the ω-1*S* and ω-2*R* positions. These findings underscore the importance of substrate positioning within the active site in determining product selectivity. Comparisons with two related P450s, $P450_{BM3}$ and $P450_{SP\alpha}$, further highlighted the critical role of active site architecture and substrate positioning in modulating selectivity. While surrounding residues do not directly dictate product selectivity, they shape the active site environment and influence substrate positioning. Furthermore, our analysis revealed a previously unrecognized catalytic role of Ala299. These findings provide a deeper mechanistic understanding of human CYP2E1 and offer valuable insights for its precise engineering in targeted C−H functionalization.

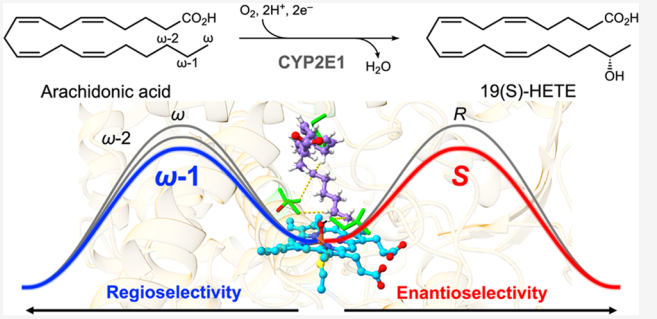

1. INTRODUCTION

Cytochrome P450 enzymes (P450s) form a superfamily of heme monooxygenases that play a crucial role in xenobiotic detoxification and the synthesis of endogenous compounds.[1−6] CYP2E1, a P450 isozyme, is essential for proper bodily function and the regulation of energy metabolism.[7−9] CYP2E1 exhibits broad substrate specificity, metabolizing alcohols, aldehydes, and both bicyclic and monocyclic compounds (e.g., benzene and caffeine), as well as long-chain fatty acids like arachidonic acid.[10,11] Due to its extensive substrate range, CYP2E1 is involved in various physiological and pathological processes, including gluconeogenesis, hepatic cirrhosis, diabetes, and obesity.[7,9,12] Induction of CYP2E1 leads to increased lipid peroxidation and apoptosis, which elevate blood-brain barrier permeability and contribute to neurodegeneration.[7,13] When metabolizing polyunsaturated fatty acids like arachidonic acid, CYP2E1 generates reactive oxygen species and toxic metabolites in the liver.[9,14] These reactive intermediates damage lipids, proteins, and DNA, leading to inflammation and liver fibrosis.[9] Moreover, CYP2E1-mediated oxidative stress has been implicated in insulin resistance and metabolic disorders such as type 2 diabetes and obesity.[15]

To date, six crystal structures have been determined for human CYP2E1—three with bound fatty acids and three with other small molecules.[16−19] CYP2E1 exhibits the typical P450 architecture, consisting of 12 α-helices (A−L) and four β-sheets (β1−β4).[16] Notably, CYP2E1's active site is relatively compact compared to other human P450s (Figure 1a).[16,17] This compactness is primarily due to the protrusion of an isoleucine

Received: January 18, 2025
Revised: January 23, 2025
Accepted: January 24, 2025
Published: February 11, 2025

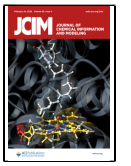

https://doi.org/10.1021/acs.jcim.5c00115
J. Chem. Inf. Model. 2025, 65, 2080−2092

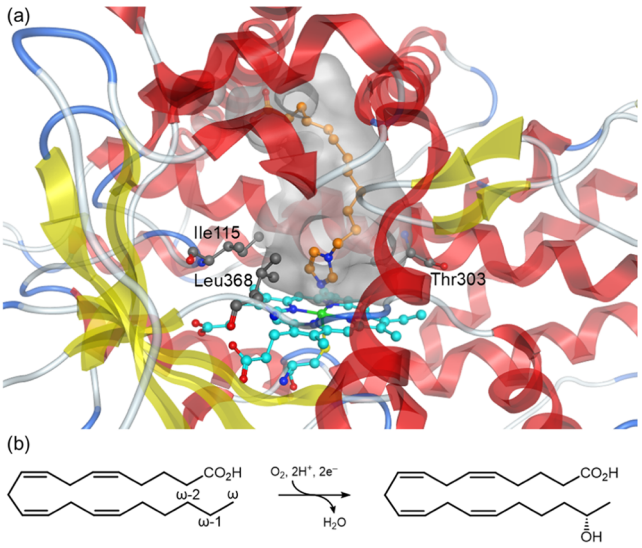

Figure 1. (a) Active-site structure of CYP2E1 with ω-imidazolyl-dodecanoic acid bound as a ligand (PDB ID 3LC4). The gray surface highlights the available space for the ligand. (b) Chemical structures of arachidonic acid and its major metabolite in CYP2E1 metabolism. The terminal atoms are labeled according to the ω system, where ω designates the terminal CH_3 group of the fatty acid chain.

residue (I115), which restricts the catalytic space.[17,20] Additionally, T303 helps orient the substrate toward the iron site.[16] L368, along with adjacent residues, forms a narrow, hydrophobic channel, enhancing the enzyme's specificity for small hydrophobic molecules and fatty acids. Porubsky et al. investigated CYP2E1's interaction with fatty acid analogs through cocrystallization with ω-imidazolyl-octanoic, ω-imidazolyl-decanoic, and ω-imidazolyl-dodecanoic fatty acids, demonstrating that despite its initially compact nature, the active site of CYP2E1 can adapt to accommodate fatty acids.[17]

Experimental data indicate that CYP2E1 hydroxylates fatty acids, predominantly at the ω-1 position (Figure 1b).[11,21−24] In the case of arachidonic acid, CYP2E1 catalyzes the production of hydroxyeicosatetraenoic acids (HETEs), specifically 19-HETE, 18-HETE, and 20-HETE.[8,22,25] These metabolites play key physiological roles in regulating inflammation, vascular tone, and blood pressure.[26−29] The hydroxylation of arachidonic acid introduces a chiral center, producing two enantiomers (R and S) for each HETE metabolite. Notably, 19(S)-HETE, a major product (Figure 1b), has demonstrated cardioprotective effects against angiotensin II-induced cellular hypertrophy in vitro, compared to 19(R)-HETE.[27] Additionally, 18(R)-HETE has been shown to cause renal vasodilation. Gas chromatography−mass spectrometry analysis revealed that CYP2E1-produced 19-HETE consists of 70% 19(S)-HETE and 30% 19(R)-HETE, while 18-HETE is composed entirely of the R isomer.

Although computational studies have explored CYP2E1's interactions with small substrates, such as acetaldehyde, toluene, and indazole,[20,30−36] the enzymatic mechanisms underlying the fatty acid hydroxylation, particularly regarding regioselectivity and enantioselectivity, remain incompletely understood. Computational investigations of fatty acid hydroxylation by bacterial P450s are available in the literature. For example, Dubey et al. demonstrated that Phe87 plays a crucial role in the enantioselectivity of $P450_{BM3}$, which catalyzes fatty acid hydroxylation at the ω-1, ω-2, and ω-3 positions.[37] Their molecular dynamics (MD) and quantum mechanics/molecular mechanics (QM/MM) studies suggest that the ω-1 and ω-2 positions are selectively oxidized into pro-R products, consistent with experimental findings that confirm pro-R hydroxylation at these sites.[37,38]

The influence of key active-site residues on enantioselectivity is a common feature among P450s. For example, Phe87 in $P450_{BM3}$ and Arg241 in $P450_{SP\alpha}$ are essential for substrate positioning within the active site, directly affecting the stereochemical preference of hydroxylation reactions.[37,39] Accordingly, it is reasonable to hypothesize that the stereoselectivity and enantioselectivity observed in CYP2E1's fatty acid hydroxylation are similarly governed by its active-site organization. Understanding how CYP2E1's active-site architecture controls regioselectivity and enantioselectivity could provide valuable insights for modulating CYP2E1's activity, with promising applications in drug development and metabolic engineering.

Herein, MD simulations and QM/MM calculations are employed to investigate the mechanism of arachidonic acid hydroxylation catalyzed by human CYP2E1. Our findings reveal that specific active-site interactions, particularly involving residues Phe207, Thr303, Ile115, and Ala299, play a critical role in substrate binding and positioning. Notably, the ω-1S and ω-2R sites of the substrate are positioned near the reactive iron(IV)-oxo moiety of the compound I (Cpd I) intermediate, resulting in relatively low activation energy barriers and more efficient hydroxylation at these sites. By analyzing energy contributions to barrier heights, the study further identifies key factors influencing reactivity and selectivity. These insights advance our understanding of CYP2E1's catalytic mechanism, providing a foundation for the rational design of enzymes with improved catalytic properties.

2. COMPUTATIONAL METHODS

2.1. Molecular Docking. A crystal structure of human CYP2E1 (PDB ID 3LC4), complexed with ω-imidazolyl-dodecanoic acid, was downloaded from the RCSB Protein Data Bank (PDB).[19] The crystal structure was imported into the Molecular Operating Environment (MOE) v2022.02,[40] where water molecules were removed and missing residues were added. The structure of arachidonic acid was obtained from the PubChem database,[41] and the torsional freedom of the ligand's bonds was enabled to allow for the exploration of various conformations within the active site during the docking process.[40] The ligand was placed in the active site of human CYP2E1 using the coordinates of ω-imidazolyl-dodecanoic acid in the crystal structure as a reference.[17] This placement was performed using the Proxy Triangle method, with the resulting poses ranked by the London dG scoring function.[40,42−45] By integrating these approaches, the docking simulations effectively accounted for the ligand's high flexibility, ensuring that the predicted binding modes were both realistic and reliable.[46−50] A total of 100 high-scoring complex geometries were generated, from which three poses (poses 1−3), showing similarities to the binding mode of ω-imidazolyl-dodecanoic acid in the crystal structure, were selected for subsequent MD simulations.[17]

2.2. MD Simulations. The three selected docking poses of arachidonic acid in complex with CYP2E1 were used as initial coordinates for 100 ns all-atom MD simulations using AMBER20 software. The protonation states of the residues were determined based on the pK_a values of amino acids, estimated using H++ software, and through visual inspection of local hydrogen bonding networks. Histidine residues His109,

https://doi.org/10.1021/acs.jcim.5c00115
J. Chem. Inf. Model. 2025, 65, 2080−2092

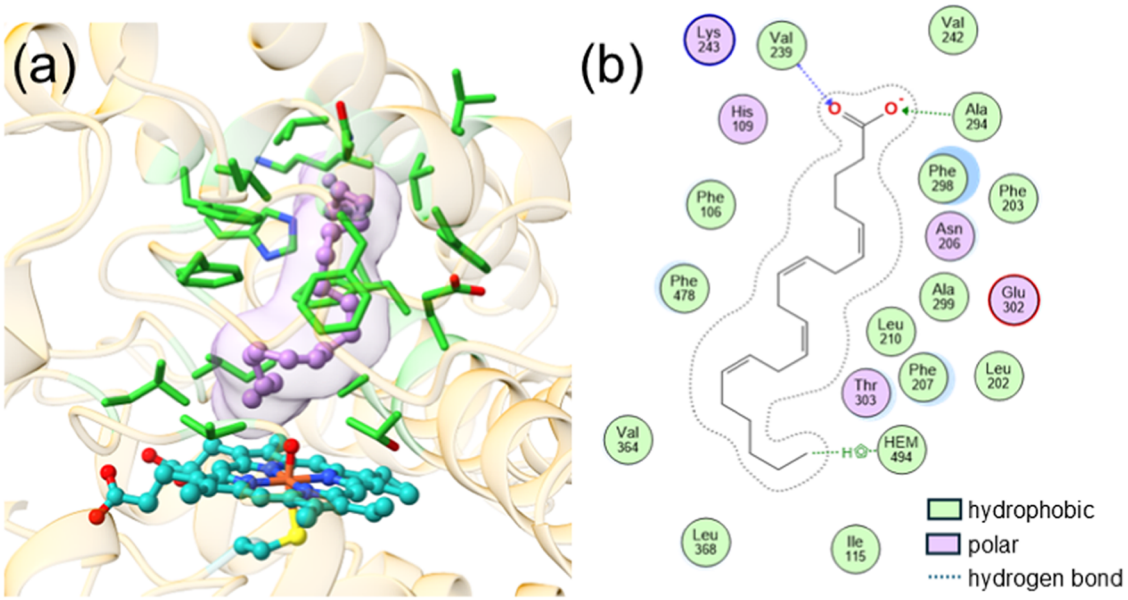

Figure 2. (a) Three-dimensional and (b) two-dimensional visualizations of the complex between CYP2E1 and arachidonic acid in pose 1.

His226, His355, His370, and His475 were assumed as neutral with a proton at the δ position, while His81, His107, His152, His208, His232, His254, His278, and His457 were neutral with a proton at the ε position. His188, His253, His326, and His413 were set as doubly protonated. All Asp and Glu residues, as well as the cysteine bound to the heme iron, were deprotonated. The Amber ff19SB force field was applied to the amino acid residues,[51] while force-field parameters for arachidonic acid were generated using the generalized AMBER force field (GAFF) with the antechamber module of AMBER20.[52,53] Two Cl^- ions were added to neutralize the system's charge, and the protein−ligand complex was solvated in a cubic box of a 10 Å layer of OPC water.

After the setup, MD simulations were conducted in four stages. The first stage involved initial energy minimization, starting with 5000 steps of the steepest descent algorithm followed by 5000 steps of the conjugate gradient algorithm. The system was then heated from 0 to 300 K under the NVT ensemble, using a Langevin thermostat and applying a 25 kcal/(mol·Å^2) force constant to restrain all heavy atoms, maintaining the original protein folding. In the third stage, a five-step equilibration process was performed, with each step consisting of 200,000 steps (200 ps). The restraining force was progressively reduced across the five stages (25, 15, 5, 2.5, and 0.2 kcal/(mol·Å^2)), under the NPT ensemble at 1.013 bar and 300 K. This was followed by a 1 ns equilibration run in the NPT ensemble without restraints. In the fourth stage, 100 ns MD simulations were performed under the NPT ensemble. Long-range electrostatic interactions were calculated using the Particle Mesh Ewald algorithm. Three independent 100 ns MD simulations were performed for each system, with random initial velocities. After the simulations, the trajectories were classified based on which carbon or hydrogen atom in arachidonic acid was closest to the oxo group in Cpd I. The binding free energy between the protein and ligand was then evaluated using the Molecular Mechanics Poisson−Boltzmann Surface Area (MM-PBSA) method. The MMPBSA.py tool from the AMBER20 package was employed to gain insights into the binding affinities and energetics of the arachidonic acid−CYP2E1 interactions.

2.3. QM/MM Calculations. QM/MM methods have become invaluable tools for studying enzyme-catalyzed reactions, offering insights that bridge experimental findings with atomic-level interactions.[47,54−67] These calculations now extend to complex biological systems, including human P450s.[46,47,68] A subtractive QM/MM approach, ONIOM-(QM:MM), was employed to explore the mechanistic details of arachidonic acid metabolism in CYP2E1. To randomly select an initial structure for QM/MM calculations from the MD trajectory, a snapshot with the lowest total energy was chosen. Only water molecules within a 10 Å radius of arachidonic acid were retained. The doublet spin state was assumed for all calculations.

Two-layer ONIOM calculations were performed to determine the geometries and energetics of the reactants, intermediates, transition states (TSs), and products.[69−71] All ONIOM calculations were performed using Gaussian 16.[72] The ONIOM method defines two different-sized systems within the entire system, the real system and the model system. The real system is treated with a lower level of theory, while the model system, a smaller subset of the real system, is treated with both lower and higher levels of theory. The total ONIOM energy, E_{ONIOM}, is calculated as

$$E_{\mathrm{ONIOM}} = E_{\mathrm{low,real}} + E_{\mathrm{high,model}} - E_{\mathrm{low,model}} \quad (1)$$

In our calculations, the model system included porphine, the iron-oxo unit, the side chain of the axial cysteine ligand, and the terminal five carbon atoms of arachidonic acid, along with their corresponding hydrogen atoms. Gaussian-default AMBER and TIP3P parameters were utilized for all MM calculations. The TIP3P water model was chosen in ONIOM calculations for its simplicity in describing electrostatic interactions and its seamless implementation within the Gaussian program.[72] The same force-field parameters, used for the above MD simulations, were specifically applied to arachidonic acid and the heme group. The ONIOM mechanical embedding (ONIOM-ME) approach, in combination with the B3LYP/6-31G* QM method, was used for geometry optimization calculations.[73−76] The energy derived from this ONIOM framework is referred to as $E1$. Additionally, frequency calculations were performed at

https://doi.org/10.1021/acs.jcim.5c00115
J. Chem. Inf. Model. 2025, 65, 2080−2092

the same level to characterize stationary-point structures and obtain the free-energy correction values (G_{corr}). Single-point energy calculations using the electronic embedding (ONIOM-EE) scheme combined with the B3LYP/def2-TZVP method yielded ONIOM energy $E2$.[77] Furthermore, the DFT-D3BJ approach was applied to evaluate the dispersion energy (E_{disp}) of the QM atoms.[78,79] The sum of these values ($E2$, E_{disp} and G_{corr}) was used to assess the relative stability of various species.

3. RESULTS AND DISCUSSION

3.1. Binding mode of Arachidonic Acid with CYP2E1 Determined by Docking. The initial configuration of the protein−ligand complex was constructed based on the crystal structure of CYP2E1 in complex with ω-imidazolyl-dodecanoic acid (PDB code: 3LC4). In this structure, the first residue corresponds to the 31st residue in the primary sequence. While this residue is asparagine in the primary structure, it appears as lysine in the crystal structure due to the substitution of a positively charged lysine at the N-terminus to enhance expression and solubility.[80] For modeling purposes, only residues 32 to 493 were included. Under physiological conditions, the fatty acid substrate predominantly exists in its carboxylate ($-COO^-$) form. Accordingly, the deprotonated form of arachidonic acid was docked into the active site of CYP2E1.

Based on the docking results, three poses (poses 1−3) were selected for subsequent computational studies (Figures 2 and S1). These three poses share several similarities, except for the stronger hydrogen bond observed between Val239 and the hydrophilic head of arachidonic acid in pose 1. In this pose, arachidonic acid adopts a notably extended conformation as it fits into the hydrophobic cavity defined by residues such as Leu210, Phe106, Phe203, Ile115, Leu202, and Leu368. The ligand is stabilized primarily by van der Waals and hydrophobic interactions along its long aliphatic chain. Additionally, the conjugated double bonds of arachidonic acid interact through stacking with aromatic residues Phe106 and Phe478, further contributing to its stability and orientation within the active site. The carboxyl group of arachidonic acid is also stabilized through hydrogen bonding with nearby residues.

Our docking results are consistent with the findings of Hu et al., confirming phenylalanine residues, particularly Phe478, play a pivotal role in shaping the CYP2E1 catalytic pocket.[33] Furthermore, our study identified a binding mode similar to those reported for complexes with fatty acid analogs, such as ω-imidazolyl-octanoic fatty acid,[17] further reinforcing the reliability of our results.

3.2. MD Simulations Elucidate the Origin of Hydroxylation Enantioselectivity. With the complex structures obtained, MD simulations were performed to investigate the dynamic behavior and substrate-induced conformational fluctuations of the CYP2E1−ligand complex. Three independent production MD simulations were performed for each docking pose. The root-mean-square deviation (RMSD) was calculated for each system to assess structural stability.[81,82] The RMSD values of the C_α atoms and the ligand's heavy atoms were calculated relative to the initial configuration of the production simulations (Figure S2 and Table S1). As shown in Figure S2, the RMSD values of the C_α atoms of CYP2E1 were monitored over the simulation period for three independent trajectories across three distinct docking poses. For all three systems, the RMSD values of the protein tended to stabilize as the simulations progressed (Figure S2a). Among the trajectories, trajectory 3 of pose 1 exhibited relatively low RMSD values, with average values of 1.28 Å for the protein and 1.17 Å for the ligand, indicating a stable interaction network between arachidonic acid and CYP2E1 in this trajectory (Table S1). The low RMSD value of 1.17 Å for arachidonic acid can be attributed to the compact nature of the enzyme's active site,[16,17] along with strong binding affinities, both of which restrict the ligand's movement (Table S2). Similar observations of low RMSD values have been reported in studies involving strong enzyme−ligand interactions and spatial constraints, further supporting our findings.[83,84] Additionally, the stabilization of both protein and ligand RMSD values across the trajectories (Figure S2) confirms their suitability for further detailed analysis.

Following the MD simulations, the trajectories were classified based on the potential hydroxylation sites on arachidonic acid. This classification is a crucial step in determining the likely enantioselectivity of the hydroxylation process catalyzed by CYP2E1. Our analysis focused on the ω-1 and ω-2 positions, which were identified as primary sites for hydroxylation by CYP2E1.[24,29] The classification was performed using geometric criteria, analyzing each trajectory segment to assess the proximity of the ω-1 and ω-2 hydrogen atoms to Cpd I. Throughout the MD simulations, the distances between these hydrogen atoms and the Cpd I oxygen were measured. The configurations were further identified as pro-*R* and pro-*S* forms based on the Cahn−Ingold−Prelog priority rules, which assign these designations according to the priority of substituents and their spatial arrangement around chiral centers. This approach yielded distinct trajectory sets corresponding to four possible configurations (Figure 3a−d): *S*-*R* (the ω-1 hydrogen in the *S* configuration and the ω-2 hydrogen in the *R* configuration), *R*-*S* (the ω-1 hydrogen in the *R* configuration and the ω-2 hydrogen in the *S* configuration), *S*-*S* (both ω-1 and ω-2 hydrogens in the *S* configuration), and *R*-*R* (both ω-1 and ω-2 hydrogens in the *R* configuration).

Figure 3e presents the cumulative frequency of each configuration across different trajectories and poses. The data clearly indicate that the *S*-*R* configuration is predominant in most trajectories and poses, reflecting an enantioselective preference in CYP2E1-catalyzed hydroxylation. This finding aligns with a previous study demonstrating CYP2E1's strong enantioselective preference for the *S* configuration at the ω-1 site and the *R* configuration at the ω-2 site.[29] The frequency analysis further reveal variations in enantiomeric preference across trajectories. For instance, trajectory 3 of pose 1 exhibits a higher prevalence of the *S*-*R* configuration compared to trajectories 1 and 2. This correlates with the observed lower RMSD values observed for the ligand in trajectory 3, suggesting greater stability (Table S1). The predominance of the *S*-*R* configuration highlights a preferential orientation that facilitates substrate binding and promotes the progression of the reaction.

MM-PBSA binding free energy calculations were performed to further investigate the interaction energies (Table S2). The results show that pose 1, particularly trajectory 3, exhibits the strongest binding properties, primarily driven by strong van der Waals and electrostatic interactions. Porubsky et al. investigated the structural flexibility of CYP2E1 and concluded that substrate binding is driven mainly by hydrophobic interactions.[17] Hu et al. highlighted the critical role of phenylalanine residues in shaping CYP2E1's reaction environment and influencing product formation. These residues expand the cavity size to accommodate bulky substrates and regulate their orientation. This aligns with our findings, which show weaker van der Waals

https://doi.org/10.1021/acs.jcim.5c00115
J. Chem. Inf. Model. 2025, 65, 2080−2092

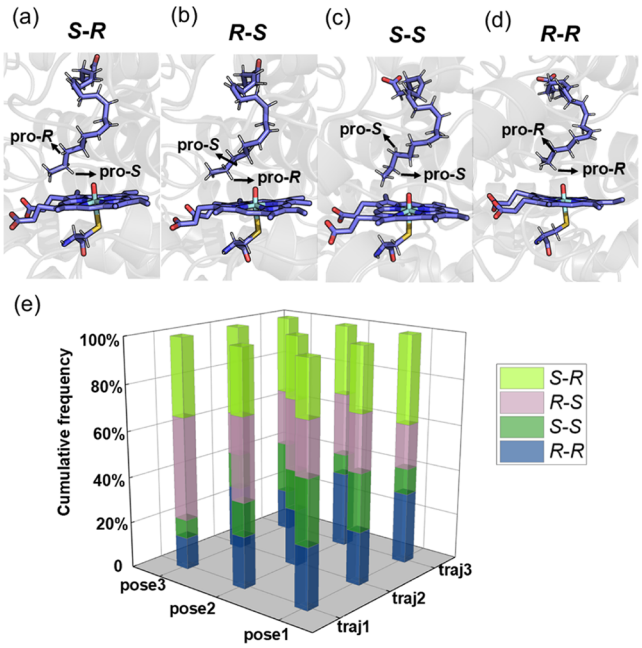

Figure 3. Classification of arachidonic acid hydroxylation configurations and their frequencies. (a–d) Structural representations of arachidonic acid within the active site of CYP2E1, illustrating the four possible configurations based on the orientations of the ω-1 and ω-2 hydrogens relative to the Cpd I oxygen. The pro-*S* and pro-*R* positions are labeled to indicate potential sites for hydrogen abstraction. (e) Cumulative frequency of each configuration (*S-R*, *R-S*, *S-S*, *R-R*) observed across different simulation poses and trajectories. The bars represent the percentage occurrence of each configuration within the specified poses and trajectories. The geometric parameters used in the analysis are the distances between the ω-1 and ω-2 hydrogen atoms and the Cpd I oxygen, with no fixed distance cutoff applied during the classification process.

interactions in the *S-S* configuration. Interestingly, a comparative study of several P450 structures also highlighted the importance of hydrophobic residues in CYP2A6 for forming a compact active site.[18]

The MM-PBSA analysis reveals that trajectory 3 of pose 1 exhibits the highest binding affinity, primarily stabilized by van der Waals and electrostatic interactions (Table S2). This trajectory predominantly comprises *S-R* and *R-R* configurations, consistent with experimental findings.[29] To gain deeper insights, trajectory 3 of pose 1 was subjected to further analysis. Building on the existing classifications (*S-R*, *R-R*, *S-S*, *R-S*), the trajectories were further categorized into ω, ω-1, and ω-2 groups (Figure 4a–c). These groups are defined based on the positions of carbon atoms relative to the oxo group of Cpd I. The ω group indicates that the carbon atom of the terminal methyl group is closest to the oxo, ω-1 refers to the carbon atom adjacent to the methyl group being nearest to the oxo, and ω-2 denotes that the third-to-last carbon atom is the closest to the oxo.

The carbon atom at the ω-1 position consistently remains in close proximity to the oxo group and is more frequently found in close proximity to it (Figure 4d,e). Further analysis of the hydrogen atoms at the ω-1*R* and ω-1*S* positions shows that the pro-*S* hydrogen atom in the ω-1 site is more often closer to the oxo moiety (Figure 4f). This proximity suggests a higher likelihood of hydrogen atom abstraction during the reaction. Similarly, the pro-*R* hydrogen atom at the ω-2 site tends to stay closer to the oxo unit, suggesting a preference for the *R* configuration at this site (Figure 4g). These results suggest a potential enantioselective preference of CYP2E1 for the *S* configuration at the ω-1 position and the *R* configuration at the ω-2 position. This aligns with experimental observations showing that CYP2E1 preferentially produces 19(*S*)-HETE and 18(*R*)-HETE.

Numerous experimental studies have demonstrated that CYP2E1 primarily functions as a ω-1 hydroxylase, supporting our computational findings.[23,24,29] However, some controversy remains regarding its activity at the ω and ω-2 positions. Tanaka et al. investigated the ω and ω-1 hydroxylation activities of purified P450 DM (rat CYP2E1) toward arachidonic acid using high-performance liquid chromatography.[85,86] Their results revealed that P450 DM hydroxylates arachidonic acid at both the ω-1 and ω positions, with a hydroxylation activity ratio of 1.22:0.50. Arnold et al. examined recombinant CYP2E1 hydroxylase activity, reporting regioisomeric product ratios of 67% for 19-HETE and 11% for 20-HETE.[11] In contrast, Laethem et al. detected only trace amounts of 20-HETE in the metabolic products. This discrepancy might arise from the similar HPLC properties of 18-HETE and 20-HETE.[29,85] Our QM/MM calculations, detailed below, assess the activation energies of hydroxylation reactions at different reaction sites, complementing the inherent limitations of MD simulations.[87]

3.3. QM/MM Analysis of Regio- and Enantioselectivity in the CYP2E1-Catalyzed Hydroxylation. *3.3.1. Hydroxylation Mechanism.* QM/MM results for the hydroxylation reaction of arachidonic acid catalyzed by CYP2E1 are summarized in Figure 5a. The energy profiles for multiple pathways (ω, ω-1*R*, ω-1*S*, ω-2*R*, and ω-2*S*) are displayed, with the energy of the reactant complex (RC, **1**) set at 0.0 kcal/mol. The H-abstraction transition state **2*** exhibits the highest energy for all pathways, confirming its rate-limiting nature: 21.9 kcal/mol for ω, 19.6 kcal/mol for ω-1*R*, 18.6 kcal/mol for ω-1*S*, 19.6 kcal/mol for ω-2*R*, and 27.0 kcal/mol for ω-2*S*. The rate-limiting role of H-abstraction and the specific energy barriers observed in our calculations align with those reported for P450-catalyzed alkane hydroxylation reactions (Table S9).[37,39,46,68,88–98] Revisiting the experimental data from Tanaka et al. and Arnold et al., we note that their observed selectivity trends correspond to relatively small energy gaps, consistent with the closely spaced energy barriers observed for ω, ω-1*R*, ω-1*S*, and ω-2*R* in our study.[11,85,86]

Our results indicate that hydrogen abstraction is most efficient via the ω-1*S* pathway. The activation energy for the (*S*)-enantiomer at the ω-1 site is indeed lower than for the (*R*)-enantiomer, which is consistent with the experimentally observed pro-*S* hydroxylation preference. At the ω-2 site, the activation energy for the (*R*)-enantiomer is significantly lower than for the (*S*)-enantiomer, in line with experimentally observed enantioselectivity.[29] The ω position, with an activation energy of 21.9 kcal/mol, presents a much higher barrier. Despite MD data showing that the ω carbon is slightly closer to the oxo moiety than the ω-2 carbon, the higher barrier for hydrogen abstraction at the ω site (2.3 kcal/mol higher than at the ω-2*R* position) makes reaction at the ω position less likely.

No significant geometric differences were observed among the TSs (**2***) of the different pathways; the breaking C–H bond and the forming O–H bond exhibit comparable bond lengths. However, the TS for the ω pathway shows a noticeably shorter O–H bond length, indicating a late TS. This suggests that the reaction is electronically less favorable. Nonetheless, the

https://doi.org/10.1021/acs.jcim.5c00115
J. Chem. Inf. Model. 2025, 65, 2080–2092

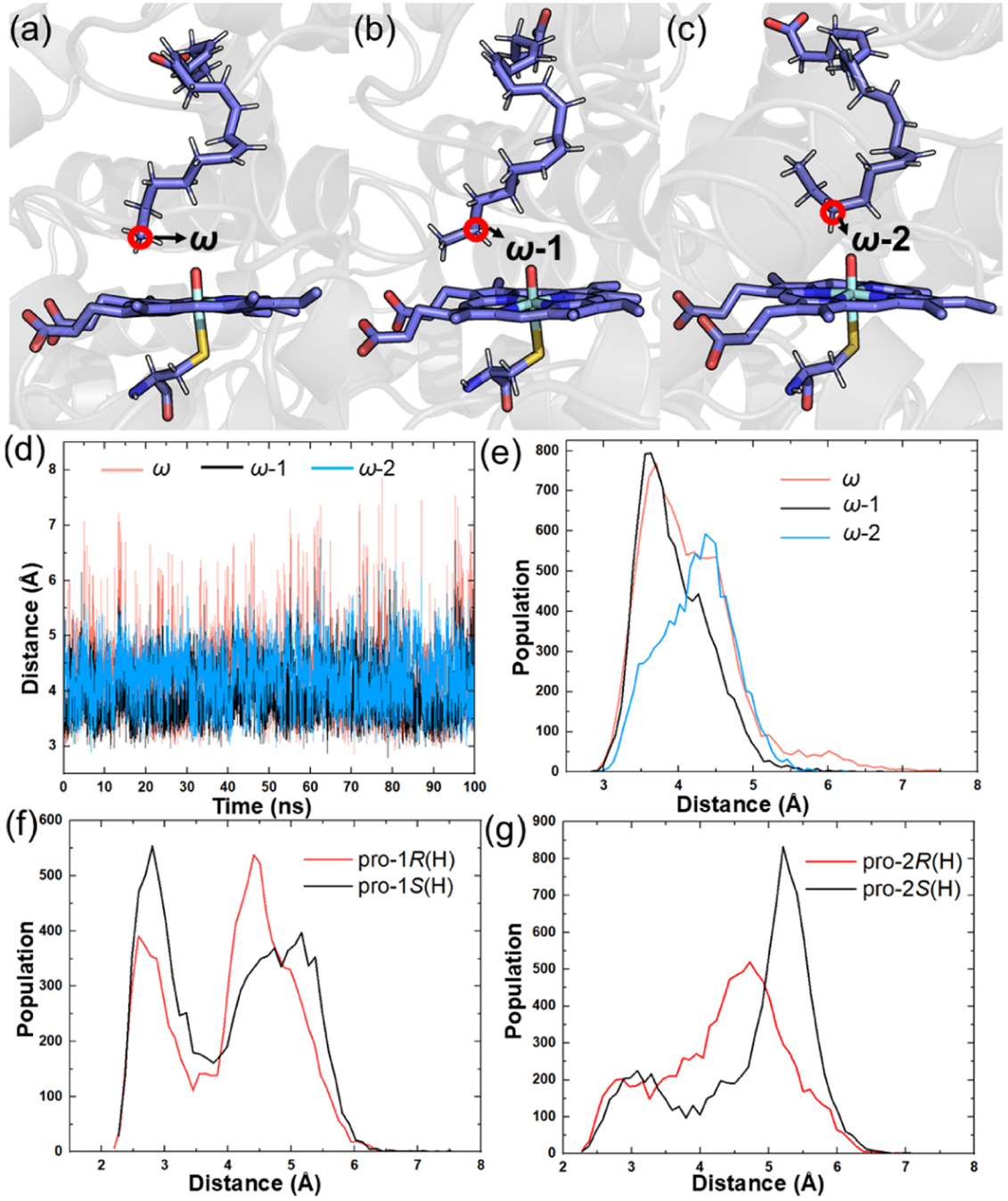

Figure 4. (a−c) Illustration of the three distinct binding configurations (ω: a, ω-1: b, ω-2: c) of arachidonic acid within the active site of CYP2E1. (d) Time evolution of the distances between the carbon atoms (ω, ω-1, ω-2 sites) of arachidonic acid and the oxo moiety of the CYP2E1 Cpd I during the MD simulation. (e) Population distribution of the distances presented in (d). The horizontal axis represents the distances between the carbon atom (ω, ω-1, or ω-2 site) of arachidonic acid and the oxo moiety of the Cpd I. (f) Population distribution of the distances between the ω-1*R* and ω-1*S* hydrogen atoms and the oxo moiety. The horizontal axis represents the distance between the ω-1*R* or ω-1*S* hydrogen atom and the oxo moiety. (g) Population distribution of the distances between the ω-2*R* and ω-2*S* hydrogen atoms and the oxo moiety. The horizontal axis represents the distance between the ω-2*R* or ω-2*S* hydrogen atom and the oxo moiety. All distances are reported in Ångstroms (Å).

reaction remains entropically favorable, as discussed below (Section 3.3.2), preventing the relative stability of this TS (21.9 kcal/mol) from becoming excessively high. Additionally, the TSs share similar electronic characteristics. During the H-abstraction step, one electron transfers from the substrate to the a_{2u}-type orbital of Cpd I. As shown in Figure 5b, despite differences in the stabilities of the TSs, their spin density values on the porphyrin ring remain nearly identical, highlighting minimal differences in electronic structure. H-abstraction leads to the formation of an intermediate (**3**) containing a substrate radical. The relative stabilities of the intermediates across different pathways are observed to approximately correlate with the relative stabilities of their corresponding TSs.

In the ω-1*S* pathway, a product complex (PC, **5**) forms without encountering a rebound barrier following the intermediate, exhibiting a low energy of −48.7 kcal/mol, which indicates substantial thermodynamic stability. Similarly, the ω-1*R* and ω-2*R* pathways yield stable PCs with energies of

https://doi.org/10.1021/acs.jcim.5c00115
J. Chem. Inf. Model. 2025, 65, 2080−2092

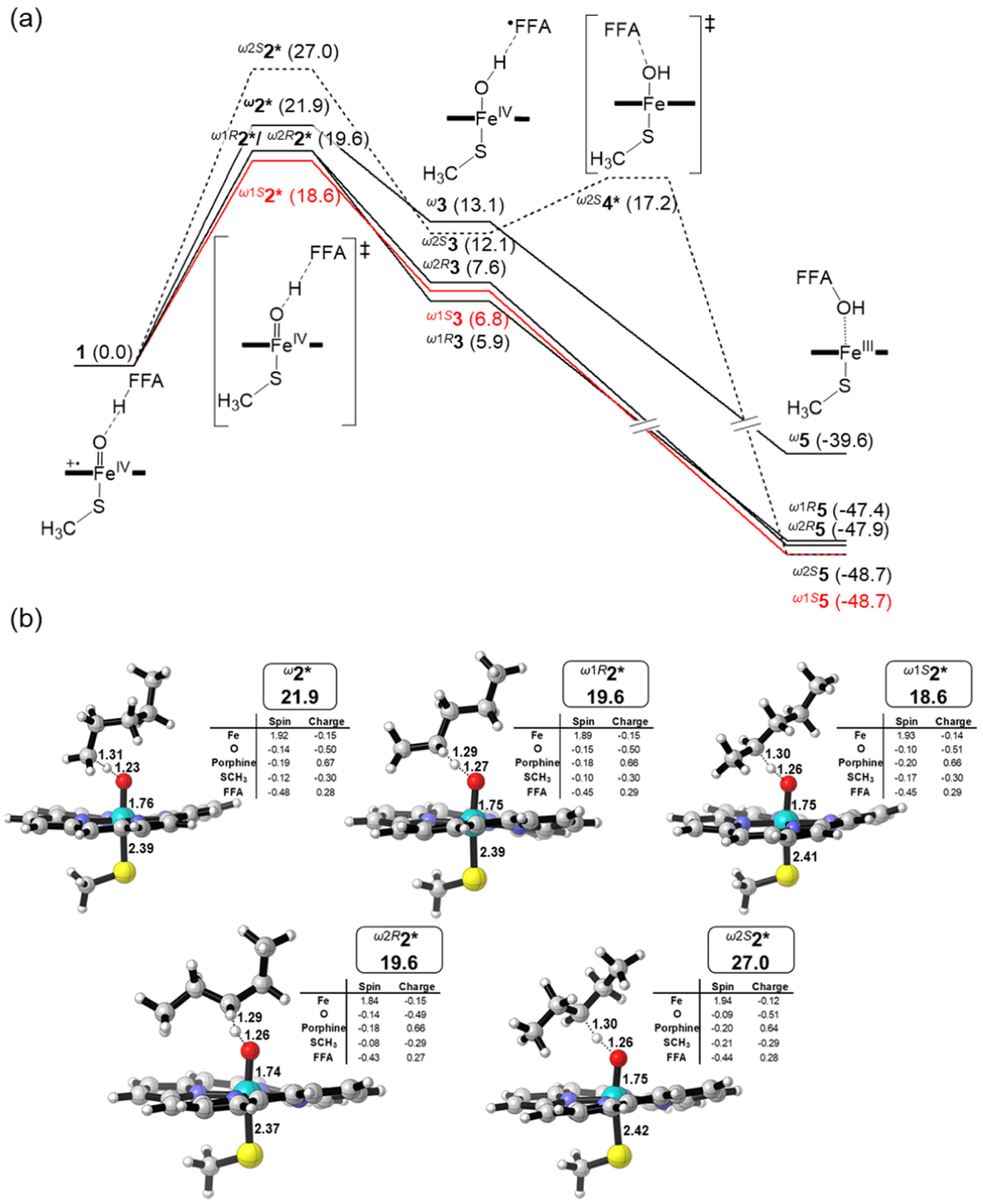

Figure 5. (a) Free energy profiles (kcal/mol) for arachidonic acid hydroxylation by CYP2E1. (b) QM/MM-optimized structures of key H-abstraction TSs. The length unit is Å. Each TS geometry is presented alongside Mulliken group spin density and charge data for the QM atoms, obtained using the ONIOM-EE(B3LYP/def2-TZVP:MM) method. The most energy-favorable pathway is presented in red. These data are shown for the following groups: Fe (heme iron); O (oxo group); porphine; SCH_3; and FFA (free fatty acid).

−47.4 and −47.9 kcal/mol, respectively. In contrast, the ω pathway produces a PC at −39.6 kcal/mol, noticeably higher in energy compared to other pathways, likely due to the primary nature of the resulting alcohol. Notably, the ω-2*S* pathway, which has the highest H-abstraction barrier, also features a significant rebound barrier for product complex formation. The instability of the TSs for both steps in this pathway is attributed to unfavorable geometric strain arising during the reaction at this site. These findings are consistent with the experimental observation of a 100% (*R*)-enantiomer at the ω-2 site.[29]

3.3.2. Origins of Regio- and Enantioselectivity in the CYP2E1-Catalyzed Hydroxylation. Variations in energy profiles across different pathways highlight the high sensitivity of CYP2E1's catalytic efficiency and selectivity to the molecular geometry of the substrate within the active site. The notably lower energy barriers in the ω-1*S*, ω-2*R*, and ω-1*R* pathways likely result from more favorable substrate positioning within the active site, contributing to selective product formation. To elucidate the origins of the regio- and enantioselectivity, we

https://doi.org/10.1021/acs.jcim.5c00115
J. Chem. Inf. Model. 2025, 65, 2080−2092

further conducted a theoretical analysis of the H-abstraction TSs. The ONIOM-based G value is decomposed into five terms

$$G = E_{QM} + E_{disp} + E_{MM} + E_{pol} + G_{corr} \quad (2)$$

where E_{QM} refers to the gas-phase energy of the QM atoms, while E_{MM} and E_{pol} denote the MM energy term and the polarization energy term, respectively.

$$E_{MM} = E_{MM,real} - E_{MM,model} \quad (3)$$

$$E_{pol} = E2(EE) - E2(ME) \quad (4)$$

Here, $E2(EE)$ and $E2(ME)$ represent ONIOM-EE and ONIOM-ME energies obtained from single-point energy calculations using the def2-TZVP basis set. The relative free energy (ΔG) of H-abstraction TS with respect to RC is decomposed into five constituent terms

$$\Delta G = \Delta E_{QM} + \Delta E_{disp} + \Delta E_{MM} + \Delta E_{pol} + \Delta G_{corr} \quad (5)$$

The results of the energy decomposition analysis (Figure 6) reveal that ΔE_{QM} is the primary determinant of the reaction barriers. Both ω-1S and ω-2R, identified as reactive sites, exhibit relatively low ΔE_{QM} values. Additionally, stabilization due to ΔE_{MM} is relatively high for the ω-1R and ω-1S pathways, indicating favorable nonbonded interactions in these pathways. Variations in ΔE_{disp} can be attributed to the distinct approaches of the substrate to Cpd I and the differences in the interaction strengths of hydrogen atoms at various positions. Specifically, hydrogen atoms at different sites on the arachidonic acid molecule approach Cpd I with slightly different orientations, influencing the dispersion forces involved. Furthermore, during reactions at different sites, arachidonic acid undergoes varying degrees of displacement, influencing substrate interactions with the surrounding protein environment and thereby altering the ΔE_{MM} term. The ΔG_{corr} term is the smallest for the ω TS, as the ω position, being at the terminal end of the arachidonic acid molecule, renders the TS at this position more flexible than others. This structural flexibility provides an entropic advantage. Additionally, ΔG_{corr} tends to become more positive—and thus more destabilizing—when ΔE_{MM} is more negative. This occurs because, when the substrate is stabilized through nonbonded interactions, the TS geometry becomes more congested, reducing structural flexibility. As a result, greater stabilization due to ΔE_{MM} is often offset by a corresponding destabilizing ΔG_{corr}. However, this offset effect is less pronounced in the ω-2S pathway, where $\Delta E_{MM} + \Delta G_{corr}$ is significantly positive, indicating entropically unfavorable nature. Overall, ΔE_{QM} is identified as the dominant factor influencing barrier heights, highlighting the importance of substrate positioning in determining product selectivity, even with substantial flexibility of arachidonic acid.

We further examined the protein environment surrounding the reacting substrate (Figure 7). Hydrophobic residues play a key role in stabilizing the TSs. Specifically, Phe207 and Thr303 serve as critical anchors for the substrate. For the ω, ω-1R, ω-1S, ω-2R, and ω-2S sites, the distances between the carbon atom at the ω position and the terminal methyl of the ethyl group of the Ile115 side chain are 3.82, 3.75, 3.76, 3.59, and 4.00 Å, respectively, highlighting the proximity of this residue to the terminal methyl. The somewhat larger values for the ω and ω-2S TS structures suggest greater substrate displacement during H-abstraction, partially disrupting this favorable interaction.

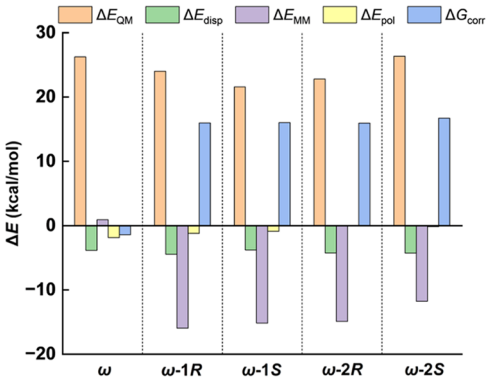

Figure 6. Comparison of different energy terms comprising ΔG (in kcal/mol) for the H-abstraction TSs.

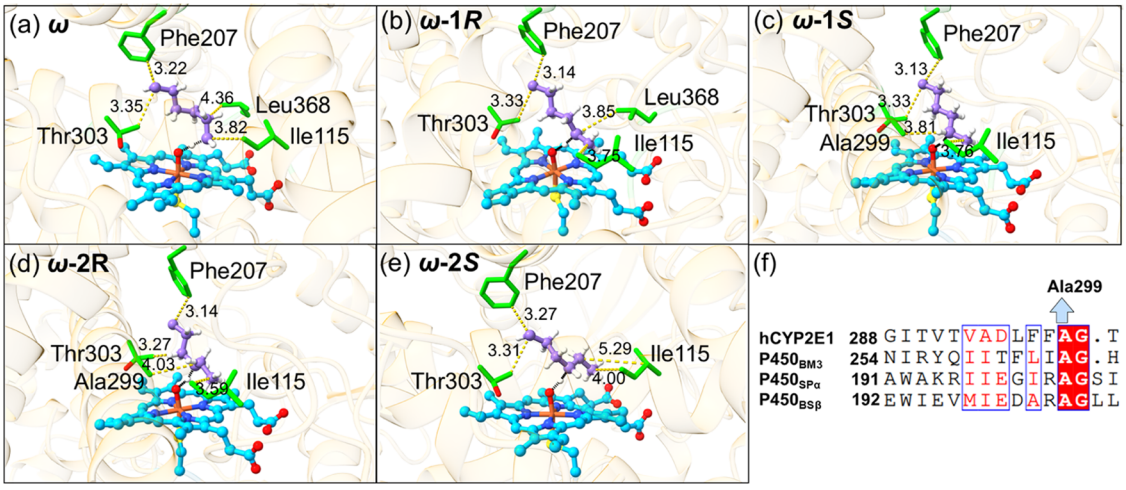

Figure 7. H-abstraction TSs for the reactions at the (a) ω, (b) ω-1R, (c) ω-1S, (d) ω-2R, and (e) ω-2S sites. (f) Sequence alignment between hCYP2E1, $P450_{BM3}$ (CYP102A1, which hydroxylates fatty acids at the CH_2 groups in the ω-1/ω-2/ω-3 positions of the hydrophobic tail), $P450_{sp\alpha}$ (CYP152B1, which hydroxylates fatty acids in an α-regioselective manner, where α is the CH_2 position adjacent to the carboxylate), and $P450_{BS\beta}$ (CYP152A1, which hydroxylates fatty acids with β regioselectivity).

https://doi.org/10.1021/acs.jcim.5c00115
J. Chem. Inf. Model. 2025, 65, 2080−2092

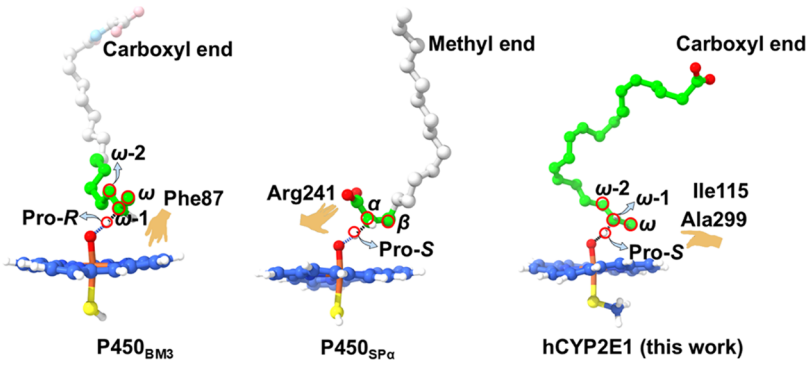

Figure 8. Schematic representation of residues controlling the regioselectivity of fatty acid oxidation by $P450_{BM3}$ (left), $P450_{SP\alpha}$ (middle), and hCYP2E1 (right).

Moreover, we observed that in the ω-1*S* and ω-2*R* TSs, the methyl carbon of the Ala299 side chain is positioned close to arachidonic acid, at distances of 3.81 and 4.03 Å, respectively, suggesting an additional stabilizing contribution that results in more negative ΔE_{MM} values. This finding is significant, as while the roles of residues Phe207 and Thr303 in enhancing the catalytic activity of CYP2E1 are well-documented for their roles, the role of Ala299 has received less attention in the literature.[33,36] Notably, sequence alignment reveals that Ala299 is conserved across various fatty acid P450 hydroxylases (Figure 7f). These results highlight a previously unrecognized role of Ala299 in facilitating substrate binding and enhancing the catalytic efficiency of CYP2E1.

3.4. Comparative Analysis of CYP2E1 with $P450_{BM3}$ and $P450_{SP\alpha}$. $P450_{BM3}$, another fatty acid hydroxylase, performs regio- and enantioselective hydroxylation of fatty acids in a manner distinctly different from CYP2E1. In $P450_{BM3}$, the ω-1, ω-2, ω-3 methylene groups of the fatty acid substrate can be hydroxylated by Cpd I, whereas the primary hydroxylation site for CYP2E1 is the ω-1 position.[99,100] What factors determine the product selectivities of these P450s, both of which act as stereoselective hydroxylases?

The primary factor distinguishing the function of $P450_{BM3}$ from CYP2E1 lies in their differing modes of substrate binding. Figure 8 illustrates the structures of H-abstraction TSs for $P450_{BM3}$, $P450_{SP\alpha}$, and human CYP2E1, with first two structures derived from previous studies.[37,39] Since the referenced structures only included partial ligand coordinates, we supplemented them using ligand structures available in PDB entries 1JPZ and 3AWM.[101,102] The added portions are shown in gray in Figure 8. In $P450_{BM3}$, the active-site residue Phe87, positioned between the heme plane and the substrate's tail, induces an upward curling of the tail through steric effects. This interaction pushes the ω end of the fatty acid substrate away from the iron(IV)-oxo moiety of Cpd I, allowing the ω-1, ω-2, and ω-3 CH_2 groups to approach Cpd I more easily. Consequently, the hydroxylation products at the ω-1, ω-2, and ω-3 CH_2 groups are distributed in the ratio of 36:30:34%.[37,100] Phe87 also plays a critical role in enantioselectivity by interacting with the fatty acid substrate. During the pro-*S* hydrogen abstraction, the substrate is drawn downward and tilts toward Phe87, leading to increased steric repulsion. This orientation raises the energy barrier for the TS compared to the pro-*R* hydrogen abstraction.[37]

In CYP2E1, Ile115, analogous to Phe87 in $P450_{BM3}$, contributes to stabilizing the TSs. Unlike phenylalanine, isoleucine in CYP2E1 lacks a phenyl ring to create steric hindrance, instead modulating regioselectivity through variations in nonbonded van der Waals interactions. Ile115 forms weaker interactions with the ω position but establishes stronger interactions at the ω-1 position. Additionally, Ala299 in CYP2E1 plays a pivotal role in enantioselectivity. The interaction between Ala299 and the substrate is strongest in the ω-1*S* TS, whereas in other states (ω, ω-1*R*, and ω-2*S*), Ala299 contributes minimally to the ligand−protein interaction.

Unlike $P450_{BM3}$ or CYP2E1, the carboxylate group of fatty acid substrates in $P450_{SP\alpha}$ forms a salt bridge with an arginine residue in the active site. This interaction positions the α-CH_2 group of the substrate near Cpd I, promoting regioselective α-hydroxylation. The pro-*R* TS experiences greater distortion than the pro-*S* TS due to partial disruption of the salt bridge with Arg241 and stronger repulsive interactions in the pro-*R* state. These factors result in a significantly higher energy barrier for the pro-*R* TS, thereby favoring pro-*S* C−H activation.[39]

In addition to the mechanisms described for $P450_{SP\alpha}$, $P450_{BM3}$ and CYP2E1, P450 OleT offers another intriguing perspective on fatty acid metabolism.[103,104] Unlike the hydroxylase activity observed in $P450_{SP\alpha}$, P450 OleT, a member of the CYP152 family, primarily catalyzes the decarboxylation of long-chain fatty acids to form terminal alkenes.[103] Lin and de Visser, using DFT calculations, demonstrated that the diversity in product distribution is closely linked to the presence of substituents at the C_α and C_β positions of the substrate.[105] Reinhard et al., through QM/MM calculations, showed that the Asn242Arg/Arg245Asn double mutant of P450 OleT modifies the active-site architecture, altering substrate orientation and thereby affecting reactivity and selectivity. This mutation reduces α-hydroxylation activity and increases the production of decarboxylation products.[106]

The influence of key active-site residues on substrate activation is a defining feature across a variety of P450s, as demonstrated in the examples discussed above.[37,39,106,107] These residues, often unique to each P450 type, play pivotal roles in shaping the geometry and electronic properties of the active site, thereby directly impacting the enzyme's catalytic specificity and efficiency. Consequently, the product selectivity of P450s is largely governed by the configuration of the active site and its critical residues, which orient substrates in specific ways. Through evolutionary refinement of their active-site architectures, different P450 members have developed functional diversity, particularly in substrate specificity and product selectivity.

https://doi.org/10.1021/acs.jcim.5c00115
J. Chem. Inf. Model. 2025, 65, 2080−2092

4. CONCLUSIONS

MD simulations and QM/MM calculations provided valuable insights into the mechanism of regio- and enantioselective fatty acid hydroxylation by human CYP2E1. The MD results indicate that hydrogen atoms at the ω-1*S* and ω-2*R* positions are closer to the reactive oxygen atom, suggesting potential sites of higher reactivity. According to QM/MM results, the ω-1*S* transition state has the lowest energy barrier, indicating the most favorable hydrogen abstraction, consistent with experimentally observed enantioselectivity. Additionally, a previously unrecognized role of Ala299 in the binding and catalysis of fatty acid substrates was identified. Comparisons between CYP2E1 and the other fatty acid hydroxylases, $P450_{BM3}$ and $P450_{SP\alpha}$, revealed that these enzymes display distinct hydroxylation profiles due to differences in substrate binding and active site interactions. The observed conformational differences, along with energy decomposition analysis, underscore the importance of substrate positioning in determining the regioselectivity and enantioselectivity of fatty acid hydroxylation. The ability to engineer P450s with enhanced regio- and stereoselectivity holds significant promise for synthetic biology and pharmaceutical chemistry. By identifying specific factors governing transition-state stability—particularly the effect of substrate positioning—this work establishes a foundation for the rational design of P450s tailored for industrial and therapeutic use.

■ ASSOCIATED CONTENT

Data Availability Statement

All crystal structures used in our study are accessible from the Protein Data Bank (https://www.rcsb.org/). The software packages employed in this work are available either freely or commercially from their respective vendors or institutions, and the references for all of them are provided in the main text.

Supporting Information

The Supporting Information is available free of charge at https://pubs.acs.org/doi/10.1021/acs.jcim.5c00115.

Additional methodological details, MD simulation results, ONIOM calculation results, group spin density data, group charge data, references, and XYZ coordinates of the optimized geometric structures for QM atoms (PDF)
Docking (ZIP)
MD (ZIP)
QM/MM (ZIP)

■ AUTHOR INFORMATION

Corresponding Author

Hajime Hirao − *Warshel Institute for Computational Biology, School of Medicine, The Chinese University of Hong Kong, Shenzhen, Guangdong 518172, P. R. China;* orcid.org/0000-0002-8239-3471; Phone: +86-0755-23519030; Email: hirao@cuhk.edu.cn

Author

Honghui Zhang − *Warshel Institute for Computational Biology, School of Medicine, The Chinese University of Hong Kong, Shenzhen, Guangdong 518172, P. R. China*

Complete contact information is available at: https://pubs.acs.org/10.1021/acs.jcim.5c00115

Author Contributions

H.Z. carried out the computational studies, generated the data, and performed the analysis. H.H. supervised the project. Both authors contributed to the writing and revision of the manuscript.

Funding

The authors gratefully acknowledge Ganghong Young Scholar Development Fund, the Changjiang Scholarship, the Guangdong Pearl River Talent Program, the Shenzhen Natural Science Foundation 2022 fund, and the funding for the Warshel Institute for Computational Biology from Shenzhen City and Longgang District (C10120180043, LGKCSDPT2024001).

Notes

The authors declare no competing financial interest.

■ REFERENCES

(1) Denisov, I. G.; Makris, T. M.; Sligar, S. G.; Schlichting, I. Structure and Chemistry of Cytochrome P450. *Chem. Rev.* **2005**, *105*, 2253−2278.
(2) Esteves, F.; Rueff, J.; Kranendonk, M. The Central Role of Cytochrome P450 in Xenobiotic Metabolism-a Brief Review on a Fascinating Enzyme Family. *J. Xenobiot.* **2021**, *11*, 94−114.
(3) McIntosh, J. A.; Farwell, C. C.; Arnold, F. H. Expanding P450 Catalytic Reaction Space through Evolution and Engineering. *Curr. Opin. Chem. Biol.* **2014**, *19*, 126−134.
(4) Fasan, R. Tuning P450 Enzymes as Oxidation Catalysts. *ACS Catal.* **2012**, *2*, 647−666.
(5) Ortiz de Montellano, P. R. Hydrocarbon Hydroxylation by Cytochrome P450 Enzymes. *Chem. Rev.* **2010**, *110*, 932−948.
(6) Guengerich, F. P. Common and Uncommon Cytochrome P450 Reactions Related to Metabolism and Chemical Toxicity. *Chem. Res. Toxicol.* **2001**, *14*, 611−650.
(7) Garcia, W. A.; Ramos-Chavez, L. A.; Rubio-Osornio, M.; Calvillo-Velasco, M.; Atzin, J. A.; Guevara, J.; Silva-Adaya, D. The Role of CYP2E1 in the Drug Metabolism or Bioactivation in the Brain. *Oxid. Med. Cell. Longevity* **2017**, *2017*, No. 4680732.
(8) Westphal, C.; Konkel, A.; Schunck, W. H. CYP-Eicosanoids–a New Link between Omega-3 Fatty Acids and Cardiac Disease? *Prostaglandins Other Lipid Mediators* **2011**, *96*, 99−108.
(9) Harjumäki, R.; Pridgeon, C. S.; Ingelman-Sundberg, M. CYP2E1 in Alcoholic and Non-Alcoholic Liver Injury. Roles of Ros, Reactive Intermediates and Lipid Overload. *Int. J. Mol. Sci.* **2021**, *22*, No. 8221.
(10) Harrelson, J. P.; Henne, K. R.; Alonso, D. O.; Nelson, S. D. A Comparison of Substrate Dynamics in Human CYP2E1 and CYP2A6. *Biochem. Biophys. Res. Commun.* **2007**, *352*, 843−849.
(11) Arnold, C.; Markovic, M.; Blossey, K.; Wallukat, G.; Fischer, R.; Dechend, R.; Konkel, A.; von Schacky, C.; Luft, F. C.; Muller, D. N.; Rothe, M.; Schunck, W. H. Arachidonic Acid-Metabolizing Cytochrome P450 Enzymes Are Targets of Omega-3 Fatty Acids. *J. Biol. Chem.* **2010**, *285*, 32720−32733.
(12) Zhang, Y.; Yan, T.; Wang, T.; Liu, X.; Hamada, K.; Sun, D.; Sun, Y.; Yang, Y.; Wang, J.; Takahashi, S.; Wang, Q.; Krausz, K. W.; Jiang, C.; Xie, C.; Yang, X.; Gonzalez, F. J. Crosstalk between CYP2E1 and PPARα Substrates and Agonists Modulate Adipose Browning and Obesity. *Acta Pharm. Sin. B* **2022**, *12*, 2224−2238.
(13) Haorah, J.; Knipe, B.; Leibhart, J.; Ghorpade, A.; Persidsky, Y. Alcohol-Induced Oxidative Stress in Brain Endothelial Cells Causes Blood-Brain Barrier Dysfunction. *J. Leukocyte Biol.* **2005**, *78*, 1223−1232.
(14) Leclercq, I. A.; Farrell, G. C.; Field, J.; Bell, D. R.; Gonzalez, F. J.; Robertson, G. R. CYP2E1 and CYP4A as Microsomal Catalysts of Lipid Peroxides in Murine Nonalcoholic Steatohepatitis. *J. Clin. Invest.* **2000**, *105*, 1067−1075.
(15) Zong, H.; Armoni, M.; Harel, C.; Karnieli, E.; Pessin, J. E. Cytochrome P450 CYP2E1 Knockout Mice Are Protected against High-Fat Diet-Induced Obesity and Insulin Resistance. *Am. J. Physiol.: Endocrinol. Metab.* **2012**, *302*, E532−E539.
(16) Porubsky, P. R.; Meneely, K. M.; Scott, E. E. Structures of Human Cytochrome P450 2E1. Insights into the Binding of Inhibitors and Both

Small Molecular Weight and Fatty Acid Substrates. *J. Biol. Chem.* **2008**, *283*, 33698−33707.
(17) Porubsky, P. R.; Battaile, K. P.; Scott, E. E. Human Cytochrome P450 2E1 Structures with Fatty Acid Analogs Reveal a Previously Unobserved Binding Mode. *J. Biol. Chem.* **2010**, *285*, 22282−22290.
(18) DeVore, N. M.; Meneely, K. M.; Bart, A. G.; Stephens, E. S.; Battaile, K. P.; Scott, E. E. Structural Comparison of Cytochromes P450 2A6, 2A13, and 2E1 with Pilocarpine. *FEBS J.* **2012**, *279*, 1621−1631.
(19) Burley, S. K.; Bhikadiya, C.; Bi, C.; Bittrich, S.; Chen, L.; Crichlow, G. V.; Christie, C. H.; Dalenberg, K.; Di Costanzo, L.; Duarte, J. M.; Dutta, S.; Feng, Z.; Ganesan, S.; Goodsell, D. S.; Ghosh, S.; Green, R. K.; Guranović, V.; Guzenko, D.; Hudson, B. P.; Lawson, C. L.; Liang, Y.; Lowe, R.; Namkoong, H.; Peisach, E.; Persikova, I.; Randle, C.; Rose, A.; Rose, Y.; Sali, A.; Segura, J.; Sekharan, M.; Shao, C.; Tao, Y. P.; Voigt, M.; Westbrook, John D.; Young, J. Y.; Zardecki, C.; Zhuravleva, M. Rcsb Protein Data Bank: Powerful New Tools for Exploring 3d Structures of Biological Macromolecules for Basic and Applied Research and Education in Fundamental Biology, Biomedicine, Biotechnology, Bioengineering and Energy Sciences. *Nucleic Acids Res.* **2021**, *49*, D437−D451.
(20) Wu, X.; Chen, Y.; Wang, X.; Wei, W.; Liang, Y. Origin of Site Selectivity in Toluene Hydroxylation by Cytochrome P450 Enzymes. *J. Org. Chem.* **2021**, *86*, 13768−13773.
(21) Adas, F.; Berthou, F.; Picart, D.; Lozac, P.; Beaugé, F.; Amet, Y. Involvement of Cytochrome P450 2E1 in the (ω−1)-Hydroxylation of Oleic Acid in Human and Rat Liver Microsomes. *J. Lipid Res.* **1998**, *39*, 1210−1219.
(22) Adas, F.; Salaün, J. P.; Berthou, F.; Picart, D.; Simon, B.; Amet, Y. Requirement for ω and (ω−1)-Hydroxylations of Fatty Acids by Human Cytochromes P450 2E1 and 4A11. *J. Lipid Res.* **1999**, *40*, 1990−1997.
(23) Fukuda, T.; Imai, Y.; Komori, M.; Nakamura, M.; Kusunose, E.; Kusunose, M. Replacement of Thr303 of P450 2E1 with Serine Modifies the Regioselectivity of Its Fatty Acid Hydroxylase Activity. *J. Biochem.* **1993**, *113*, 7−12.
(24) Fukuda, T.; Imai, Y.; Komori, M.; Nakamura, M.; Kusunose, E.; Satouchi, K.; Kusunose, M. Different Mechanisms of Regioselection of Fatty Acid Hydroxylation by Laurate (ω-1)-Hydroxylating P450s, P450 2C2 and P450 2E1. *J. Biochem.* **1994**, *115*, 338−344.
(25) El-Sherbeni, A. A.; El-Kadi, A. O. Characterization of Arachidonic Acid Metabolism by Rat Cytochrome P450 Enzymes: The Involvement of CYP1As. *Drug Metab. Dispos.* **2014**, *42*, 1498−1507.
(26) Rocic, P.; Schwartzman, M. L. 20-HETE in the Regulation of Vascular and Cardiac Function. *Pharmacol. Ther.* **2018**, *192*, 74−87.
(27) Elkhatali, S.; El-Sherbeni, A. A.; Elshenawy, O. H.; Abdelhamid, G.; El-Kadi, A. O. 19-Hydroxyeicosatetraenoic Acid and Isoniazid Protect against Angiotensin II-Induced Cardiac Hypertrophy. *Toxicol. Appl. Pharmacol.* **2015**, *289*, 550−559.
(28) Yu, J.; Zhu, H.; Kindy, M. S.; Taheri, S. Cytochrome P450 CYP2E1 Suppression Ameliorates Cerebral Ischemia Reperfusion Injury. *Antioxidants* **2021**, *10*, No. 52.
(29) Laethem, R. M.; Balazy, M.; Falck, J. R.; Laethem, C. L.; Koop, D. R. Formation of 19(S)-, 19(R)-, and 18(R)-Hydroxyeicosatetraenoic Acids by Alcohol-Inducible Cytochrome P450 2E1. *J. Biol. Chem.* **1993**, *268*, 12912−12918.
(30) Li, J.; Wei, D.; Wang, J.; Yu, Z.; Chou, K. Molecular Dynamics Simulations of CYP2E1. *Med. Chem.* **2012**, *8*, 208−221.
(31) Li, J.; Wei, D. Q.; Wang, J. F.; Li, Y. X. A Negative Cooperativity Mechanism of Human CYP2E1 Inferred from Molecular Dynamics Simulations and Free Energy Calculations. *J. Chem. Inf. Model.* **2011**, *51*, 3217−3225.
(32) Shen, Z.; Cheng, F.; Xu, Y.; Fu, J.; Xiao, W.; Shen, J.; Liu, G.; Li, W.; Tang, Y. Investigation of Indazole Unbinding Pathways in CYP2E1 by Molecular Dynamics Simulations. *PLoS One* **2012**, *7*, No. e33500.
(33) Hu, K.; Tu, H.; Xie, J.; Yang, Z.; Li, Z.; Chen, Y.; Liu, Y. Phenylalanine Residues in the Active Site of CYP2E1 Participate in Determining the Binding Orientation and Metabolism-Dependent Genotoxicity of Aromatic Compounds. *Toxics* **2023**, *11*, No. 495.
(34) Wang, Y.; Wang, H.; Wang, Y.; Yang, C.; Yang, L.; Han, K. Theoretical Study of the Mechanism of Acetaldehyde Hydroxylation by Compound I of CYP2E1. *J. Phys. Chem. B* **2006**, *110*, 6154−6159.
(35) Jaladanki, C. K.; Khatun, S.; Gohlke, H.; Bharatam, P. V. Reactive Metabolites from Thiazole-Containing Drugs: Quantum Chemical Insights into Biotransformation and Toxicity. *Chem. Res. Toxicol.* **2021**, *34*, 1503−1517.
(36) Lu, Q.; Song, J.; Wu, P.; Li, C.; Thiel, W. Mechanistic Insights into the Directing Effect of Thr303 in Ethanol Oxidation by Cytochrome P450 2E1. *ACS Catal.* **2019**, *9*, 4892−4901.
(37) Dubey, K. D.; Wang, B.; Shaik, S. Molecular Dynamics and QM/MM Calculations Predict the Substrate-Induced Gating of Cytochrome P450 BM3 and the Regio- and Stereoselectivity of Fatty Acid Hydroxylation. *J. Am. Chem. Soc.* **2016**, *138*, 837−845.
(38) Capdevila, J. H.; Wei, S.; Helvig, C.; Falck, J. R.; Belosludtsev, Y.; Truan, G.; Graham-Lorence, S. E.; Peterson, J. A. The Highly Stereoselective Oxidation of Polyunsaturated Fatty Acids by Cytochrome P450BM3. *J. Biol. Chem.* **1996**, *271*, 22663−22671.
(39) Ramanan, R.; Dubey, K. D.; Wang, B.; Mandal, D.; Shaik, S. Emergence of Function in P450-Proteins: A Combined Quantum Mechanical/Molecular Mechanical and Molecular Dynamics Study of the Reactive Species in the H_2O_2-Dependent Cytochrome $P450_{SP\alpha}$ and Its Regio- and Enantioselective Hydroxylation of Fatty Acids. *J. Am. Chem. Soc.* **2016**, *138*, 6786−6797.
(40) Chemical Computing Group ULC. *Molecular Operating Environment (MOE)*; S. S. W.: Suite #910, Montreal, QC, Canda, H3A 2R7, 2023.
(41) Kim, S.; Thiessen, P. A.; Bolton, E. E.; Chen, J.; Fu, G.; Gindulyte, A.; Han, L.; He, J.; He, S.; Shoemaker, B.; Wang, J.; Yu, B.; Zhang, J.; Bryant, S. H. Pubchem Substance and Compound Databases. *Nucleic Acids Res.* **2016**, *44*, D1202−D1213.
(42) Vilar, S.; Cozza, G.; Moro, S. Medicinal Chemistry and the Molecular Operating Environment (MOE): Application of QSAR and Molecular Docking to Drug Discovery. *Curr. Top. Med. Chem.* **2008**, *8*, 1555−1572.
(43) Zaheer, H.; Halim, S. A.; Uddin, R.; Madura, J. D. Benchmarking Docking and Scoring Protocol for the Identification of Potential Acetylcholinesterase Inhibitors. *J. Mol. Graphics Modell.* **2010**, *28*, 870−882.
(44) Nawaz, M. Z.; Attique, S. A.; Ain, Q.; Alghamdi, H. A.; Bilal, M.; Yan, W.; Zhu, D. Discovery and Characterization of Dual Inhibitors of Human Vanin-1 and Vanin-2 Enzymes through Molecular Docking and Dynamic Simulation-Based Approach. *Int. J. Biol. Macromol.* **2022**, *213*, 1088−1097.
(45) Sarwar, M. W.; Riaz, A.; Dilshad, S. M. R.; Al, A.; Nawaz, M. S.; Mubin, M. Structure Activity Relationship (SAR) and Quantitative Structure Activity Relationship (QSAR) Studies Showed Plant Flavonoids as Potential Inhibitors of Dengue NS2B-NS3 Protease. *BMC Struct. Biol.* **2018**, *18*, No. 6.
(46) Yue, D.; Ng, E. W. H.; Hirao, H. Hydrogen-Bond-Assisted Catalysis: Hydroxylation of Paclitaxel by Human CYP2C8. *J. Am. Chem. Soc.* **2024**, *146*, 30117−30125.
(47) Yue, D.; Hirao, H. Mechanism of Selective Aromatic Hydroxylation in the Metabolic Transformation of Paclitaxel Catalyzed by Human CYP3A4. *J. Chem. Inf. Model.* **2023**, *63*, 7826−7836.
(48) Wright, J. S.; Anderson, J. M.; Shadnia, H.; Durst, T.; Katzenellenbogen, J. A. Experimental Versus Predicted Affinities for Ligand Binding to Estrogen Receptor: Iterative Selection and Rescoring of Docked Poses Systematically Improves the Correlation. *J. Comput.-Aided. Mol. Des.* **2013**, *27*, 707−721.
(49) Waqas, M.; Ullah, S.; Halim, S. A.; Rehman, N. U.; Ali, A.; Jan, A.; Muhsinah, A. B.; Khan, A.; Al, A. Targeting Papain-Like Protease by Natural Products as Novel Therapeutic Potential SARS-CoV-2. *Int. J. Biol. Macromol.* **2024**, *258*, No. 128812.
(50) Fouad, M. A.; Osman, A. A.; Abdelhamid, N. M.; Rashad, M. W.; Nabawy, A. Y.; El Kerdawy, A. M. Discovery of Dual Kinase Inhibitors Targeting VEGFR2 and FAK: Structure-Based Pharmacophore Modeling, Virtual Screening, and Molecular Docking Studies. *BMC Chem.* **2024**, *18*, No. 29.

https://doi.org/10.1021/acs.jcim.5c00115
J. Chem. Inf. Model. 2025, 65, 2080−2092

(51) Tian, C.; Kasavajhala, K.; Belfon, K. A.; Raguette, L.; Huang, H.; Migues, A. N.; Bickel, J.; Wang, Y.; Pincay, J.; Wu, Q.; Simmerling, C. ff19SB: Amino-Acid-Specific Protein Backbone Parameters Trained against Quantum Mechanics Energy Surfaces in Solution. *J. Chem. Theory Comput.* **2020**, *16*, 528−552.
(52) Wang, J.; Wolf, R. M.; Caldwell, J. W.; Kollman, P. A.; Case, D. A. Development and Testing of a General Amber Force Field. *J. Comput. Chem.* **2004**, *25*, 1157−1174.
(53) Case, D. A.; B, K.; Ben-Shalom, I. Y.; Brozell, S. R.; Cerutti, D. S.; Cheatham, T. E., III; Cruzeiro, V.W.D.; Darden, T. A.; Duke, R. E.; Giambasu, G.; Gilson, M. K.; Gohlke, H.; Goetz, A. W.; Harris, R.; Izadi, S.; Izmailov, S. A.; Kasavajhala, K.; Kovalenko, A.; Krasny, R.; Kurtzman, T.; Lee, T. S.; LeGrand, S.; Li, P.; Lin, C.; Liu, J.; Luchko, T.; Luo, R.; Man, V.; Merz, K. M.; Miao, Y.; Mikhailovskii, O.; Monard, G.; Nguyen, H.; Onufriev, A.; Pan, F.; Pantano, S.; Qi, R.; Roe, D. R.; Roitberg, A.; Sagui, C.; Schott-Verdugo, S.; Shen, J.; Simmerling, C. L.; Skrynnikov, N. R.; Smith, J.; Swails, J.; Walker, R. C.; Wang, J.; Wilson, L.; Wolf, R. M.; Wu, X.; Xiong, Y.; Xue, Y.; York, D. M.; Kollman, P. A. *Amber 2020*; University of California: San Francisco, 2020.
(54) Zhao, F.; Moriwaki, Y.; Noguchi, T.; Shimizu, K.; Kuzuyama, T.; Terada, T. QM/MM Study of the Catalytic Mechanism and Substrate Specificity of the Aromatic Substrate C-Methyltransferase Fur6. *Biochemistry* **2024**, *63*, 806−814.
(55) Hu, F.; Wang, Y.; Zeng, J.; Deng, X.; Xia, F.; Xu, X. Unveiling the State Transition Mechanisms of Ras Proteins through Enhanced Sampling and QM/MM Simulations. *J. Phys. Chem. B* **2024**, *128*, 1418−1427.
(56) Boneta, S.; Arafet, K.; Moliner, V. QM/MM Study of the Enzymatic Biodegradation Mechanism of Polyethylene Terephthalate. *J. Chem. Inf. Model.* **2021**, *61*, 3041−3051.
(57) Meelua, W.; Wanjai, T.; Thinkumrob, N.; Friedman, R.; Jitonnom, J. Multiscale QM/MM Simulations Identify the Roles of Asp239 and 1-OH···Nucleophile in Transition State Stabilization in Arabidopsis Thaliana Cell-Wall Invertase 1. *J. Chem. Inf. Model.* **2023**, *63*, 4827−4838.
(58) Jitonnom, J.; Mujika, J. I.; Kamp, M. W.; Mulholland, A. J. Quantum Mechanics/Molecular Mechanics Simulations Identify the Ring-Opening Mechanism of Creatininase. *Biochemistry* **2017**, *56*, 6377−6388.
(59) Meelua, W.; Wanjai, T.; Thinkumrob, N.; Oláh, J.; Mujika, J. I.; Ketudat-Cairns, J. R.; Hannongbua, S.; Jitonnom, J. Active Site Dynamics and Catalytic Mechanism in Arabinan Hydrolysis Catalyzed by GH43 Endo-Arabinanase from QM/MM Molecular Dynamics Simulation and Potential Energy Surface. *J. Biomol. Struct. Dyn.* **2022**, *40*, 7439−7449.
(60) Senn, H. M.; Thiel, W. QM/MM Methods for Biomolecular Systems. *Angew. Chem., Int. Ed.* **2009**, *48*, 1198−1229.
(61) Senn, H. M.; Thiel, W. QM/MM Studies of Enzymes. *Curr. Opin. Chem. Biol.* **2007**, *11*, 182−187.
(62) Lin, H.; Truhlar, D. G. QM/MM: What Have We Learned, Where Are We, and Where Do We Go from Here? *Theor. Chem. Acc.* **2007**, *117*, 185−199.
(63) Mulholland, A. J. Modelling Enzyme Reaction Mechanisms, Specificity and Catalysis. *Drug Discovery Today* **2005**, *10*, 1393−1402.
(64) Ruiz-Pernía, J. J.; Świderek, K.; Bertran, J.; Moliner, V.; Tuñón, I. Electrostatics as a Guiding Principle in Understanding and Designing Enzymes. *J. Chem. Theory Comput.* **2024**, *20*, 1783−1795.
(65) Sousa, S. F.; Ribeiro, A. J.; Neves, R. P.; Brás, N. F.; Cerqueira, N. M.; Fernandes, P. A.; Ramos, M. J. Application of Quantum Mechanics/Molecular Mechanics Methods in the Study of Enzymatic Reaction Mechanisms. *WIREs Comput. Mol. Sci.* **2017**, *7*, No. e1281.
(66) Quesne, M. G.; Borowski, T.; de Visser, S. P. Quantum Mechanics/Molecular Mechanics Modeling of Enzymatic Processes: Caveats and Breakthroughs. *Chem. - Eur. J.* **2016**, *22*, 2562−2581.
(67) Acevedo, O.; Jorgensen, W. L. Advances in Quantum and Molecular Mechanical (QM/MM) Simulations for Organic and Enzymatic Reactions. *Acc. Chem. Res.* **2010**, *43*, 142−151.
(68) Lonsdale, R.; Houghton, K. T.; Żurek, J.; Bathelt, C. M.; Foloppe, N.; de Groot, M. J.; Harvey, J. N.; Mulholland, A. J. Quantum Mechanics/Molecular Mechanics Modeling of Regioselectivity of Drug Metabolism in Cytochrome P450 2C9. *J. Am. Chem. Soc.* **2013**, *135*, 8001−8015.
(69) Chung, L. W.; Sameera, W.; Ramozzi, R.; Page, A. J.; Hatanaka, M.; Petrova, G. P.; Harris, T. V.; Li, X.; Ke, Z.; Liu, F.; Li, H. B.; Ding, L.; Morokuma, K. The ONIOM Method and Its Applications. *Chem. Rev.* **2015**, *115*, 5678−5796.
(70) Meelua, W.; Thinkumrob, N.; Saparpakorn, P.; Pengthaisong, S.; Hannongbua, S.; Cairns, J. R. K.; Jitonnom, J. Structural Basis for Inhibition of a GH116 β-Glucosidase and Its Missense Mutants by GBA2 Inhibitors: Crystallographic and Quantum Chemical Study. *Chem.-Biol. Interact.* **2023**, *384*, No. 110717.
(71) Tue-ngeun, P.; Rakitikul, W.; Thinkumrob, N.; Hannongbua, S.; Meelua, W.; Jitonnom, J. Binding Interactions and in Silico ADME Prediction of Isoconessimine Derivatives as Potent Acetylcholinesterase Inhibitors. *J. Mol. Graphics Modell.* **2024**, *129*, No. 108746.
(72) Frisch, M. J.; Trucks, G. W.; Schlegel, H. B.; Scuseria, G. E.; Robb, M. A.; Cheeseman, J. R.; Scalmani, G.; Barone, V.; Petersson, G. A.; Nakatsuji, H.; Li, X.; Caricato, M.; Marenich, A. V.; Bloino, J.; Janesko, B. G.; Gomperts, R.; Mennucci, B.; Hratchian, H. P.; Ortiz, J. V.; Izmaylov, A. F.; Sonnenberg, J. L.; Williams; Ding, F.; Lipparini, F.; Egidi, F.; Goings, J.; Peng, B.; Petrone, A.; Henderson, T.; Ranasinghe, D.; Zakrzewski, V. G.; Gao, J.; Rega, N.; Zheng, G.; Liang, W.; Hada, M.; Ehara, M.; Toyota, K.; Fukuda, R.; Hasegawa, J.; Ishida, M.; Nakajima, T.; Honda, Y.; Kitao, O.; Nakai, H.; Vreven, T.; Throssell, K.; Montgomery, J. A., Jr.; Peralta, J. E.; Ogliaro, F.; Bearpark, M. J.; Heyd, J. J.; Brothers, E. N.; Kudin, K. N.; Staroverov, V. N.; Keith, T. A.; Kobayashi, R.; Normand, J.; Raghavachari, K.; Rendell, A. P.; Burant, J. C.; Iyengar, S. S.; Tomasi, J.; Cossi, M.; Millam, J. M.; Klene, M.; Adamo, C.; Cammi, R.; Ochterski, J. W.; Martin, R. L.; Morokuma, K.; Farkas, O.; Foresman, J. B.; Fox, D. J. *Gaussian 16*, Rev. C.01; Gaussian Inc.: Wallingford, CT, 2016.
(73) Hehre, W. J.; Ditchfield, R.; Pople, J. Self-Consistent Molecular Orbital Methods. XII. Further Extensions of Gaussian-Type Basis Sets for Use in Molecular Orbital Studies of Organic Molecules. *J. Chem. Phys.* **1972**, *56*, 2257−2261.
(74) Becke, A. D. Density-Functional Thermochemistry. III. The Role of Exact Exchange. *J. Chem. Phys.* **1993**, *98*, 5648−5652.
(75) Vosko, S. H.; Wilk, L.; Nusair, M. Accurate Spin-Dependent Electron Liquid Correlation Energies for Local Spin Density Calculations: A Critical Analysis. *Can. J. Phys.* **1980**, *58*, 1200−1211.
(76) Lee, C.; Yang, W.; Parr, R. G. Development of the Colle-Salvetti Correlation-Energy Formula into a Functional of the Electron Density. *Phys. Rev. B* **1988**, *37*, No. 785.
(77) Weigend, F.; Ahlrichs, R. Balanced Basis Sets of Split Valence, Triple Zeta Valence and Quadruple Zeta Valence Quality for H to Rn: Design and Assessment of Accuracy. *Phys. Chem. Chem. Phys.* **2005**, *7*, 3297−3305.
(78) Becke, A. D.; Johnson, E. R. A Density-Functional Model of the Dispersion Interaction. *J. Chem. Phys.* **2005**, *123*, No. 154101.
(79) Grimme, S.; Ehrlich, S.; Goerigk, L. Effect of the Damping Function in Dispersion Corrected Density Functional Theory. *J. Comput. Chem.* **2011**, *32*, 1456−1465.
(80) Scott, E. E.; Spatzenegger, M.; Halpert, J. R. A Truncation of 2B Subfamily Cytochromes P450 Yields Increased Expression Levels, Increased Solubility, and Decreased Aggregation While Retaining Function. *Arch. Biochem. Biophys.* **2001**, *395*, 57−68.
(81) Chen, J.; Chen, H.; Shi, Y.; Hu, F.; Lao, X.; Gao, X.; Zheng, H.; Yao, W. Probing the Effect of the Non-Active-Site Mutation Y229W in New Delhi Metallo-β-Lactamase-1 by Site-Directed Mutagenesis, Kinetic Studies, and Molecular Dynamics Simulations. *PLoS One* **2013**, *8*, No. e82080.
(82) Rungruangmaitree, R.; Phoochaijaroen, S.; Chimprasit, A.; Saparpakorn, P.; Pootanakit, K.; Tanramluk, D. Structural Analysis of the Coronavirus Main Protease for the Design of Pan-Variant Inhibitors. *Sci. Rep.* **2023**, *13*, No. 7055.
(83) Meduru, H.; Wang, Y. T.; Tsai, J. J.; Chen, Y. C. Finding a Potential Dipeptidyl Peptidase-4 (DPP-4) Inhibitor for Type-2 Diabetes Treatment Based on Molecular Docking, Pharmacophore

https://doi.org/10.1021/acs.jcim.5c00115
J. Chem. Inf. Model. 2025, 65, 2080−2092

Generation, and Molecular Dynamics Simulation. *Int. J. Mol. Sci.* **2016**, *17*, No. 920.
(84) Londhe, A. M.; Gadhe, C. G.; Lim, S. M.; Pae, A. N. Investigation of Molecular Details of Keap1-Nrf2 Inhibitors Using Molecular Dynamics and Umbrella Sampling Techniques. *Molecules* **2019**, *24*, No. 4085.
(85) Tanaka, S.; Imaoka, S.; Kusunose, E.; Kusunose, M.; Maekawa, M.; Funae, Y. ω- and (ω−1) -Hydroxylation of Arachidonic Acid, Lauric Acid and Prostaglandin A1 by Multiple Forms of Cytochrome P450 Purified from Rat Hepatic Microsomes. *Biochim. Biophys. Acta* **1990**, *1043*, 177−181.
(86) Imaoka, S.; Yamaguchi, Y.; Funae, Y. Induction and Regulation of Cytochrome P450 K-5 (Lauric Acid Hydroxylase) in Rat Renal Microsomes by Starvation. *Biochim. Biophys. Acta* **1990**, *1036*, 18−23.
(87) Mokkawes, T.; de Visser, S. P. Caffeine Biodegradation by Cytochrome P450 1A2. What Determines the Product Distributions? *Chem. - Eur. J.* **2023**, *29*, No. e202203875.
(88) Hui, C.; Singh, W.; Quinn, D.; Li, C.; Moody, T. S.; Huang, M. Regio- and Stereoselectivity in the CYP450$_{BM3}$-Catalyzed Hydroxylation of Complex Terpenoids: A QM/MM Study. *Phys. Chem. Chem. Phys.* **2020**, *22*, 21696−21706.
(89) Tian, L.; Friesner, R. A. QM/MM Simulation on P450 BM3 Enzyme Catalysis Mechanism. *J. Chem. Theory Comput.* **2009**, *5*, 1421−1431.
(90) Lonsdale, R.; Harvey, J. N.; Mulholland, A. J. Effects of Dispersion in Density Functional Based Quantum Mechanical/Molecular Mechanical Calculations on Cytochrome P450 Catalyzed Reactions. *J. Chem. Theory Comput.* **2012**, *8*, 4637−4645.
(91) Altun, A.; Shaik, S.; Thiel, W. What Is the Active Species of Cytochrome P450 During Camphor Hydroxylation? QM/MM Studies of Different Electronic States of Compound I and of Reduced and Oxidized Iron−Oxo Intermediates. *J. Am. Chem. Soc.* **2007**, *129*, 8978−8987.
(92) Viciano, I.; Castillo, R.; Marti, S. QM/MM Modeling of the Hydroxylation of the Androstenedione Substrate Catalyzed by Cytochrome P450 Aromatase (CYP19A1). *J. Comput. Chem.* **2015**, *36*, 1736−1747.
(93) Shaik, S.; Lai, W.; Chen, H.; Wang, Y. The Valence Bond Way: Reactivity Patterns of Cytochrome P450 Enzymes and Synthetic Analogs. *Acc. Chem. Res.* **2010**, *43*, 1154−1165.
(94) Shaik, S.; Kumar, D.; de Visser, S. P. A Valence Bond Modeling of Trends in Hydrogen Abstraction Barriers and Transition States of Hydroxylation Reactions Catalyzed by Cytochrome P450 Enzymes. *J. Am. Chem. Soc.* **2008**, *130*, 10128−10140.
(95) Kamachi, T.; Yoshizawa, K. A Theoretical Study on the Mechanism of Camphor Hydroxylation by Compound I of Cytochrome P450. *J. Am. Chem. Soc.* **2003**, *125*, 4652−4661.
(96) de Visser, S. P.; Ogliaro, F.; Sharma, P. K.; Shaik, S. What Factors Affect the Regioselectivity of Oxidation by Cytochrome P450? A DFT Study of Allylic Hydroxylation and Double Bond Epoxidation in a Model Reaction. *J. Am. Chem. Soc.* **2002**, *124*, 11809−11826.
(97) Ogliaro, F.; Harris, N.; Cohen, S.; Filatov, M.; de Visser, S. P.; Shaik, S. A Model "Rebound" Mechanism of Hydroxylation by Cytochrome P450: Stepwise and Effectively Concerted Pathways, and Their Reactivity Patterns. *J. Am. Chem. Soc.* **2000**, *122*, 8977−8989.
(98) de Visser, S. P.; Kumar, D.; Cohen, S.; Shacham, R.; Shaik, S. A Predictive Pattern of Computed Barriers for C−H Hydroxylation by Compound I of Cytochrome P450. *J. Am. Chem. Soc.* **2004**, *126*, 8362−8363.
(99) Miura, Y.; Fulco, A. ω-1, ω-2 and ω-3 Hydroxylation of Long-Chain Fatty Acids, Amides and Alcohols by a Soluble Enzyme System from Bacillus Megatyerium. *Biochim. Biophys. Acta* **1975**, *388*, 305−317.
(100) Dubey, K. D.; Shaik, S. Cytochrome P450−the Wonderful Nanomachine Revealed through Dynamic Simulations of the Catalytic Cycle. *Acc. Chem. Res.* **2019**, *52*, 389−399.
(101) Haines, D. C.; Tomchick, D. R.; Machius, M.; Peterson, J. A. Pivotal Role of Water in the Mechanism of P450 BM3. *Biochemistry* **2001**, *40*, 13456−13465.
(102) Fujishiro, T.; Shoji, O.; Nagano, S.; Sugimoto, H.; Shiro, Y.; Watanabe, Y. Crystal Structure of H_2O_2-Dependent Cytochrome P450$_{SP\alpha}$ with Its Bound Fatty Acid Substrate. *J. Biol. Chem.* **2011**, *286*, 29941−29950.
(103) Matthews, S.; Belcher, J. D.; Tee, K. L.; Girvan, H. M.; McLean, K. J.; Rigby, S. E.; Levy, C. W.; Leys, D.; Parker, D. A.; Blankley, R. T.; Munro, A. W. Catalytic Determinants of Alkene Production by the Cytochrome P450 Peroxygenase OleT$_{JE}$. *J. Biol. Chem.* **2017**, *292*, 5128−5143.
(104) Yadav, S.; Shaik, S.; Siddiqui, S. A.; Kalita, S.; Dubey, K. D. Local Electric Fields Dictate Function: The Different Product Selectivities Observed for Fatty Acid Oxidation by Two Deceptively Very Similar P450-Peroxygenases OleT and BSβ. *J. Chem. Inf. Model.* **2022**, *62*, 1025−1035.
(105) Lin, Y. T.; de Visser, S. P. Product Distributions of Cytochrome P450 OleT$_{JE}$ with Phenyl-Substituted Fatty Acids: A Computational Study. *Int. J. Mol. Sci.* **2021**, *22*, No. 7172.
(106) Reinhard, F. G. C.; Lin, Y. T.; Stanczak, A.; de Visser, S. P. Bioengineering of Cytochrome P450 OleT$_{JE}$: How Does Substrate Positioning Affect the Product Distributions? *Molecules* **2020**, *25*, No. 2675.
(107) Lee, D.-S.; Yamada, A.; Sugimoto, H.; Matsunaga, I.; Ogura, H.; Ichihara, K.; Adachi, S.; Park, S.; Shiro, Y. Substrate Recognition and Molecular Mechanism of Fatty Acid Hydroxylation by Cytochrome P450 from *Bacillus Subtilis*. *J. Biol. Chem.* **2003**, *278*, 9761−9767.